Velocity and Attenuation Characterization of the LIGO Site near Livingston, Louisiana

by Jan Harms and Brian O'Reilly

Abstract In April of 2009 a seismic survey utilizing explosive charges took place in Livingston parish, Louisiana. The area of the survey encompassed the location of the Laser Interferometer Gravitational-Wave Observatory (LIGO) Livingston interferometer. In this paper, we present an analysis of seismic data recorded with three of the LIGO seismometers and a geophone array that was deployed during the time of the survey. In particular, the geophone-array data are used to study the propagation of surface waves, whereas first-arrival measurements with the LIGO seismometers provide estimates of the speed of compressional seismic waves as a function of depth. We find that fundamental Rayleigh waves have a speed close to 205 m/s consistent with results from previous borehole tests and that speed of compressional waves is 1650 m/s at 25 m depth, increasing to 2300 m/s at 1 km depth. Blast spectra are further investigated to determine the Q value of the ground medium experienced by Rayleigh waves ($f > 1$ Hz) and body waves deeper underground. The estimated Q value is approximately 50 for the surface waves and exceeds a value of 190 for body waves propagating at depths below 100 m.

Introduction

Several kilometer-scale interferometric gravitational-wave (GW) detectors are currently in operation worldwide, with major upgrades already planned (Laser Interferometer Gravitational-Wave Observatory [LIGO] Scientific Collaboration, 2009; Lück, *et al.*, 2006; Acernese *et al.*, 2008; Tatsumi, 2008). Gravitational waves are generated by some of the most powerful events in the universe, including exploding stars, merging binary stars, deformed surfaces of rapidly rotating neutron stars, and sources in the early universe (Cutler and Thorne, 2002). These waves produce a small change in distance between two suspended masses. The interferometric detectors measure strain by observing the phase of laser light that is reflected between two suspended mirrors separated by several kilometers. The current strain sensitivities of the LIGO detectors are close to 10^{-23} Hz$^{-1/2}$ at 100 Hz, and design studies of future-generation detectors envision strain sensitivities of about 10^{-24} Hz$^{-1/2}$ down to 3 Hz (Hild *et al.*, 2009). The suspension systems decouple the motion, especially the horizontal motion of the mirrors, from the motion of the ground. However, seismic waves also produce perturbations of the gravity field by displacing the surface or by perturbing the density of the ground (Saulson, 1984; Hughes and Thorne, 1998; Beccaria *et al.*, 1998). There is no straightforward method to eliminate gravity perturbations that directly act on the suspended mirrors.

The most promising approach to eliminate these classical gravity perturbations (also known as Newtonian noise) from the GW data is to construct a model for these perturbations based on a measurement of the seismic field in the vicinity of the suspended mirrors (Harms *et al.*, 2009b). Which part of the seismic field qualifies as lying in the vicinity depends on the sensitivity goal and the lengths of seismic waves. Third-generation detectors will likely be sensitive to perturbations generated about three wavelengths away from the mirrors (Harms *et al.*, 2009a), which amounts to several kilometers, depending on the speed of sound and frequency. In addition, different types of waves produce different amounts of gravity perturbation. Whereas shear waves can only produce gravity perturbations at media interfaces and surfaces, compressional waves also lead to density perturbations (and therefore gravity perturbations) deep inside a homogeneous medium. Naturally, the success of this approach (i.e., modeling the Newtonian noise through seismic measurements) depends heavily on our understanding of the seismic field at the detector site, especially its dependence on local geology.

The sites of the two currently operating LIGO GW detectors in Louisiana and Washington state will also be the locations for the second-generation detectors of Advanced LIGO (Smith and LIGO, 2009) that are scheduled to start operation in 2015. According to current best estimates, these detectors will be sensitive to Newtonian noise at frequencies of 10–20 Hz. Therefore, it will be possible to test Newtonian-noise models and, potentially, to achieve a modest improvement of sensitivity if an accurate model can be constructed.

In April 2009, a geoseismic survey for oil and gas exploration was performed in the vicinity of the LIGO Livingston interferometer. The survey used 9000 explosive charges to map the deep subsurface structure of the surrounding area. Initially, our task was to estimate the impact of strong ground motion from nearby blasts on the suspension systems of the detector to protect the test masses, but we also took this unique opportunity to carry out an investigation of local geology using our own data-acquisition system. Waveforms of several thousand blasts were recorded. The results presented in this paper focus on the estimation of seismic parameters that are likely to be important in experimental and theoretical follow-up studies of seismic noise and the construction of a Newtonian-noise model.

Descriptions of the seismic experiment and the local geological setting are given in the sections Experimental Setup and Local Geology. In Analysis of Geophone-Array Data, we present the analysis of data recorded by a geophone array. The main result is an estimate of the speed of Rayleigh waves that are predicted to generate the dominant contribution to Newtonian noise at the surface. In Velocity-Depth Profile, we use STS-2 seismometers at the detector end and corner stations to analyze the body-wave travel times and generate a depth-velocity profile. In Seismic Attenuation, we estimate the attenuation of seismic waves, a result that can significantly impact the design of third-generation detectors.

Experimental Setup

The seismic signal was acquired by an array of (up to) 26 geophones (GS-20DX), and we used data from three STS-2 seismometers that are part of LIGO's data-acquisition system, which are deployed at the two end stations (referred to as EX and EY) and at the corner station (referred to as LVEA) of the two-arms interferometer (depicted as two sides of a right triangle in Fig. 1). The distance between LIGO's end stations to the corner station is about 4 km. Figure 2 shows a sketch of the geophone array. The typical distance between geophones along strings was 15 m, whereas the total area covered by the array was about 200 m × 350 m. The geophone data were recorded by a single acquisition station at the center of the array.

The survey company provided shot-hole locations and approximate blast times for a total of 6826 blasts, the locations of which are included in Figure 1. The blast times were sufficiently accurate to allow us to identify blast signals with a specific entry in the log files but not accurate enough to be used for travel-time measurements. For this purpose, LIGO's radio antenna was tuned to the radio signal used to detonate the explosive charges, taking into account an additional offset, typically in the range of a few 10 ms, that was specified in the log files.

The travel-time analysis was performed with the LIGO STS-2 data to make use of the large baseline provided by the detector stations. A total of 5578 blasts were found in the STS-2 data, all of them with known shot-hole locations.
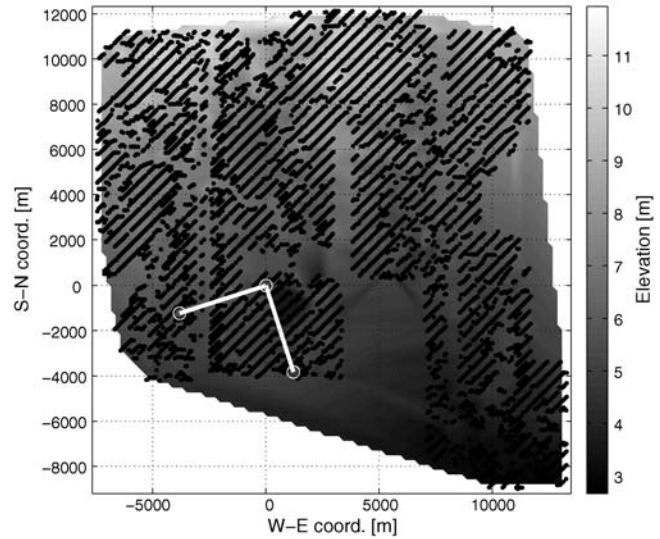
Figure 1. The area near the LIGO Livingston detector that was covered by the geoseismic survey. Each dot marks one shot hole, as provided by the log files of the survey company. The LIGO detector is sketched as two sides of a right triangle. The corner station (LVEA) coincides with the origin of the coordinate system. The detector arms have a length of about 4 km, forming a right angle. The ends of the arms are marked by the EX and EY end stations, with standard Cartesian x-y orientation. The y coordinate of the map is aligned with the north–south direction. We will later make use of the elevation profile, assuming that corrections to travel-time calculations that take into account variations in surface height can be neglected.

For 1250 of these blasts, the shot time could be determined by a simultaneous read-out of the radio signal. The geophone array was operating for two weeks; 2247 blast signals were found in the geophone data, 1829 of them with known correspondence in the STS-2 data (the remaining blasts were recorded at times when the LIGO seismometers were inoperative). Because the correspondence between blast data and log files was evaluated for the LIGO data, the geophone
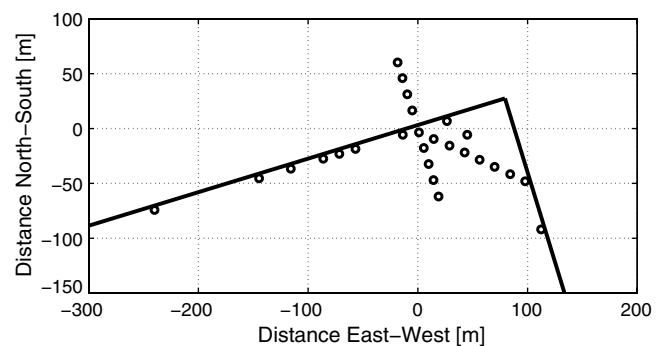
Figure 2. The geophone array was deployed near the LVEA corner station inside the area enclosed by LIGO's interferometer arms. For most of the time, the number of operating geophones was 25 or 26. The array was deployed during the blast survey so that blasts in the first days were recorded with fewer geophones. The geophone string reaching to the north was laid over one of the detector arms.

analysis presented in this paper is based on the 1829 blasts with known entries in the surveyor's logs.

Local Geology

Before the construction of the LIGO detector near Livingston, an extensive study of the near-surface ground conditions was carried out as reported in Woodward-Clyde Consultants (1995). In addition, stratification and fault systems below 900 m are known from earlier Louisiana-wide investigations published by Bebout and Gutiérrez (1983). In this section, the main characteristics of local geology relevant to this paper are summarized.

The Livingston area is part of the coastal plain in Louisiana that is divided into a series of terraces following the shoreline. The coastal plain is an elevated ocean bottom. Its topography is flat and without distinctive features. Surface outcrops consist of clays, silts, and sands deposited about 100,000 years ago, forming the Prairie Terrace Formation of the Pleistocene Series. At the LIGO site, the top 0.5–1.5 m are disturbed by logging operations. Two prominent sand-channel deposits exist. One of them is located near the LIGO corner station (LVEA), and one at the south end station (EY). Below the Pleistocene Series follow the Pliocene and upper Miocene Series, the latter one about 630–750 m below ground elevation. All series show minor spatial variation and exhibit a southward dip angle of 1°. Because the total horizontal range in the north–south direction probed by the blast survey amounts to 20 km, the depth of layers at the north and south edges of the survey area differ by about 350 m.

There are no surface or near-surface faults close to the LIGO site. Faults are found below the site in the Tuscaloosa Trend Oil and Gas Production Zone at 5,000–6,000 m depth. The nearest surface fault is the Scotlandville–Denham Springs fault, located 9–13 km south-southwest to the site.

In addition to the soil studies, the Woodward-Clyde Consultants performed one crosshole and several piezocone tests along the LIGO interferometer arms to measure seismic shear-wave speed within the first 15 m below surface. The crosshole test was a measurement between three boreholes in a row, separated by 3 m where the source was located within one of the boreholes. For the piezocone tests, a cone with three seismometers was lowered into a borehole and measured the arrival of waves that were generated at the surface. In these studies, it was found that shear-wave speed is confined within the range 160–250 m/s, with lateral variations being smaller but of similar size than vertical variation. Systematic errors especially of the piezocone tests are related to the fact that, at some of the boreholes, lower layers had smaller seismic speeds than shallow layers. (For the same reason, the accuracy of our analysis presented in the section Velocity-Depth Profile depends on the assumption that low-velocity layers do not exist at greater depths.) The seismic tests were further disturbed by reflections from ground water, which is encountered at an average depth of 2.5 m, depending strongly on the season and precipitation.

Analysis of Geophone-Array Data

Figure 3 shows a blast signal recorded by one of the geophones. The blast waveform shows the arrival of different seismic phases. The first arrival is associated with compressional waves (P waves), either in the form of direct waves or refracted waves. Later arrivals include shear waves (S waves), waves reflected from deeper layers, and the Rayleigh surface waves. The waveform shown in Figure 3 is characterized by a strongly peaked first arrival of P waves, and it clearly shows a Rayleigh wave that arrives about 6 s after the first P waves. Both features indicate that the shot hole was close to the geophone array (the distance obtained from the shot log is 1.4 km). The surface-wave arrival of more distant blasts is much later and often too weak to be visible by eye in the time series.

As a first step, we analyzed f-k maps of the blast waves. The spatial response of the geophone array is shown in Figure 4. The spatial resolution is the width of the central maximum, which is about $\delta k \approx 0.02$ m^{-1}. Irregularities of the array lead to direction dependence of the aliasing pattern and resolution. The typical distance between geophones along a string was 15 m consistent with the aliasing pattern.

Spatial amplitudes for one of the blasts are shown in Figures 5 and 6. Maps of blast waves exhibit frequency-dependent characteristics. The 5-Hz map usually shows amplitudes with a phase speed of a few hundred meters per
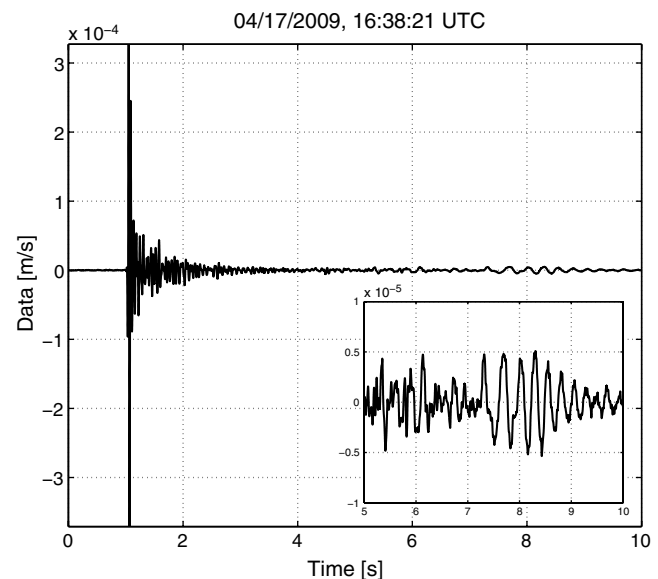

Figure 3. The shape and amplitude of the waveform indicate that the shot hole was close to the geophone array. The shot log specifies the shot-hole distance as 1.4 km. The first arrival is associated with a compressional wave. In the following 2 s, a few other arrivals can be seen that will not be specifically analyzed in this paper. Finally, starting at about 7 s, the Rayleigh surface mode becomes strongest. From the array configuration, Figure 2, and estimated arrival times at all 26 geophones, it is possible to determine the propagation direction.
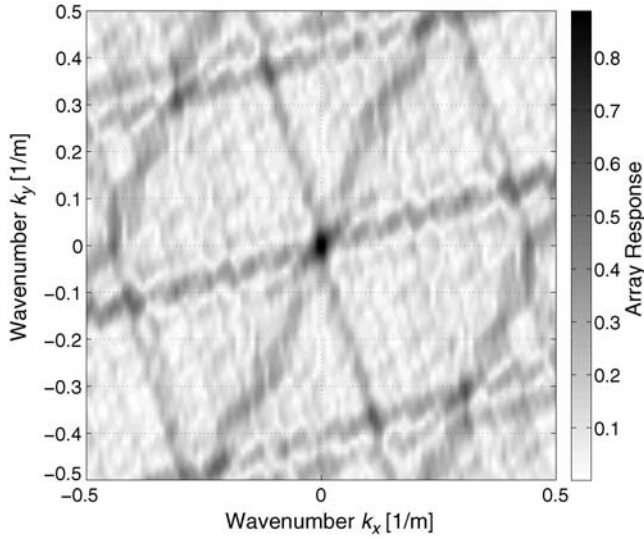
Figure 4. The response of the geophone array to plane waves, characterized by a wavenumber and horizontal propagation direction. The spatial resolution of the array corresponds to the width of the central response peak and has a value of about $\delta k \approx 0.02$ m^{-1}, which is weakly direction dependent and is determined by the size of the array. The 2D aliasing of spatial amplitudes follows a period of approximately $\Delta k \approx 0.45$ m^{-1}, which is governed by the mean distance between geophones.

second (or seismic noise for blasts with more distant shot holes). The dominant amplitude in 20-Hz maps is associated with body waves.
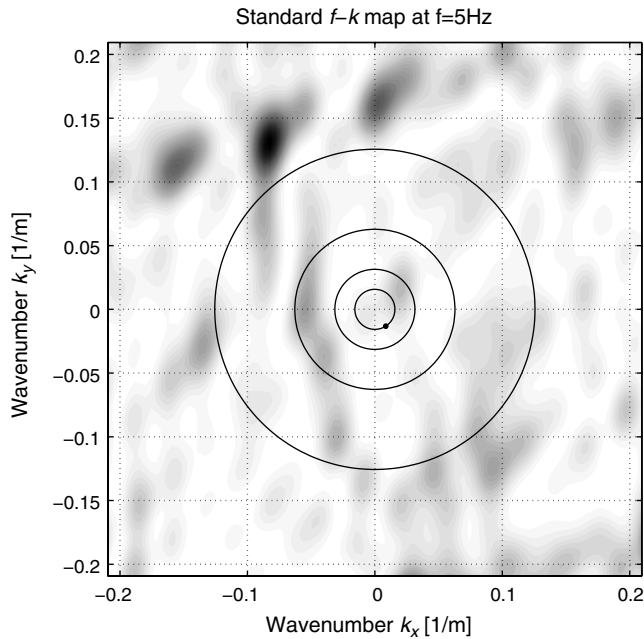
Figure 5. An f-k map at 5 Hz for the blast of Figure 3. The y axis corresponds to the north–south direction. The four circles outline (horizontal) phase speeds 2000 m/s (smallest radius), 1000 m/s, 500 m/s and 250 m/s. The map displays the Rayleigh mode with phase speed $v_h = 2\pi f/k = 200$ m/s. The dot on the innermost circle signifies the direction to the shot hole, according to the log file.
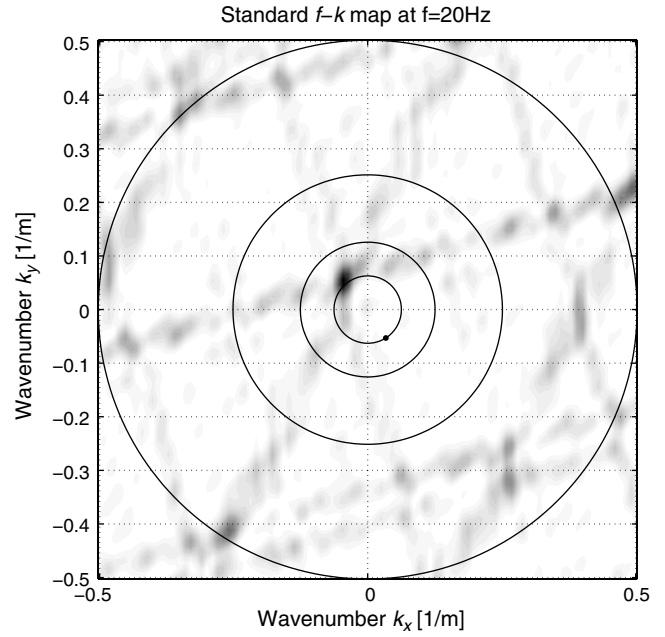
Figure 6. The 20-Hz map shows the amplitude of the body wave. The phase speed of $v_h = 1750$ m/s is typical for blasts from nearby shot holes. The aliasing pattern is visible, but it does not lead to ambiguous interpretations in this case.

As explained in Hughes and Thorne (1998), the observed speed for the first arrival of a blast wave has to be larger than the speed of compressional waves in water (about 1500 m/s) because the ground is water saturated at depths below 5–10 m, and shot holes had a depth of 25 m. This is useful prior information to check the consistency of our results. The apparent horizontal speed is determined by the distance k of the spatial amplitude to the origin of the map at frequency f according to

$$v_h = 2\pi f/k. \tag{1}$$

For better orientation, circles are drawn around the origin of all maps, indicating speeds with values of 2000, 1000, 500, and 250 m/s (the larger the circle radius, the smaller the speed). According to equation (1), the scales of the spatial spectra in Figures 5 and 6 need to be adjusted to cover similar horizontal phase speeds at different frequencies.

In order to calculate the phase speeds as a function of shot-hole distance, we first exclude all blasts whose propagation directions at any of the three frequencies (5 Hz, 10 Hz, and 20 Hz) are inconsistent with the known shot-hole azimuths to avoid contributions from seismic-noise fields, strongly scattered waves, and local disturbances. The exclusion criterion is quantified in terms of the mean-square deviation:

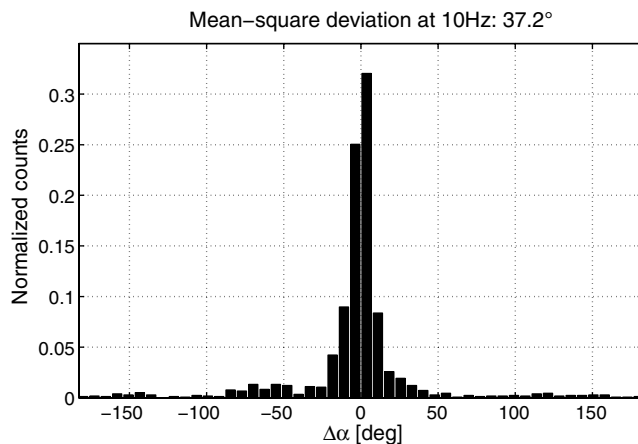$$\sigma_\alpha^2(f) = \frac{1}{B} \sum_i^B [\alpha_i(f) - \hat{\alpha}_i]^2, \tag{2}$$

where $\hat{\alpha}_i$ specifies the shot-hole back azimuth of blast i known from the blast log file; $B = 1829$ is the total number
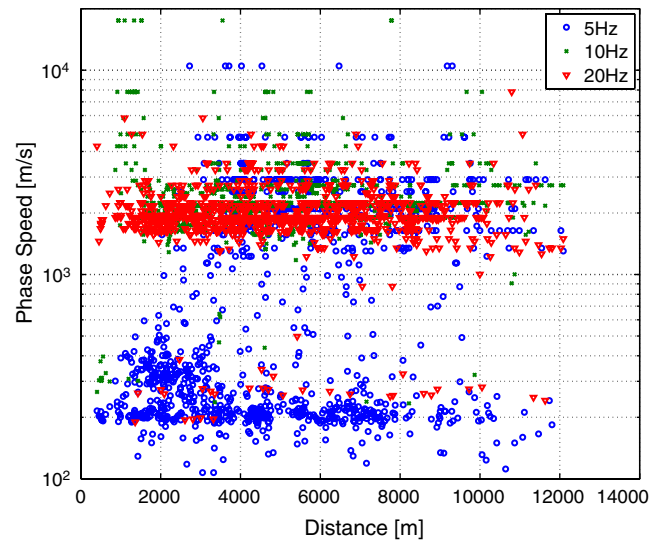
of blasts; and $\alpha_i(f)$ is the measured back azimuth of blast i, derived from its f-k map at frequency f. Note that the deviation $\Delta\alpha_i(f) \equiv \alpha_i(f) - \hat{\alpha}_i$ can have a nonvanishing mean value.

The histogram of deviations $\Delta\alpha_i(f)$ at 10 Hz is plotted in Figure 7. All blasts with $\Delta\alpha_i(f) > \sigma_\alpha(f)$ at *any* frequency are excluded. For the remaining 1055 blasts, Figure 8 shows the measured phase speeds at 5, 10, and 20 Hz as a function of distance between shot hole and geophone array. For fundamental Rayleigh waves, the (phase) speed is 205($\pm$10) m/s, and a first estimate of the speed of body waves is 2250($\pm$680) m/s at 10 Hz and 1970($\pm$520) m/s at 20 Hz. These estimates were obtained after removing outliers beyond three standard deviations (based on an initial estimate of mean and error values). The measured Rayleigh-wave speed is consistent with the near-surface shear-wave measurements in Woodward-Clyde Consultants (1995). The large estimation errors of the body-wave speeds and many of the removed outliers can be explained by strong near-surface scattering of the blast wave. In the next section (Velocity-Depth Profile), we will present an alternative analysis of compressional body waves that yield a far more accurate estimate of their speed.

Another interesting property of the 5-Hz data that should be noted is that surface waves from the closest shot holes can have a significantly higher speed than the fundamental Rayleigh mode. These waves may be associated with Rayleigh overtones that resonate within the uppermost layers of the ground, as discussed in Hughes and Thorne (1998). Unfortunately, the impact of local features on this data is too great to allow us to accurately estimate their speed.

Figure 8. Horizontal speeds for each frequency as a function of shot-hole distance to the geophone array. The observed speeds form several groups. One group consists of the surface modes with speeds between 200 and 400 m/s. Another group consists of P waves at 10 Hz and 20 Hz whose speeds lie between 1600 and 3000 m/s. Because this method is a local measurement of seismic speeds, it could be that near-surface scattering disturbs the apparent horizontal speed significantly (relative to the expected value, assuming lateral homogeneity), which would explain the absence of a trend in speed as a function of distance at 10 and 20 Hz. In the next section, we will use (nonlocal) travel-time measurements that yield better results. The color version of this figure is available only in the electronic edition.
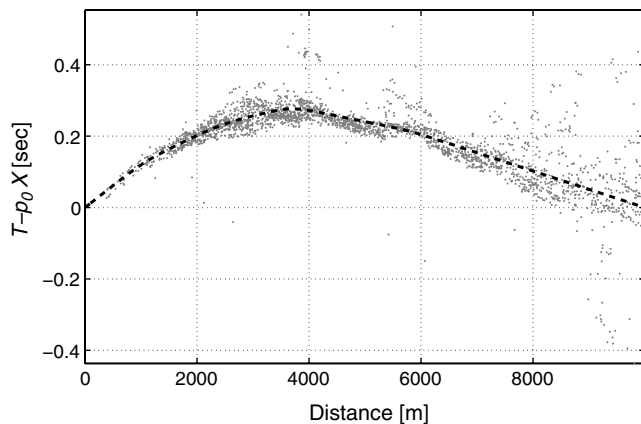
Velocity-Depth Profile

For the 1250 blasts with known shot times, travel-time data from the three STS-2 seismometers located at the corner and end-stations of the Livingston interferometer were analyzed to derive a velocity–depth profile $v(z)$, assuming lateral homogeneity. Whether lateral homogeneity can be assumed will be discussed again at the end of this section. The shot-hole depth was 25 m for all blasts, which lies below the unconsolidated uppermost layer. We simplify the problem by assuming that the ray follows a surface ($z = 0$) to surface path. The corresponding systematic error, due to neglecting the travel time of the wave through the last 25 m of the ground under the seismometer, is much smaller than typical fluctuations of the travel-time data except for shot holes closer than 1 km. The shot-hole locations are accurate to within 10 m, and the locations of our sensors are also known with better accuracy. Thus uncertainties of the horizontal travel distance are negligible and may be safely neglected. The travel-time data of all blasts measured by any of the three STS-2 are fitted to obtain a differentiable function $T(X)$—travel time versus horizontal travel distance—that determines the ray parameter

$$p(X) = \frac{dT}{dX}. \tag{3}$$

Figure 7. The distribution of deviations of propagation azimuths for 10 Hz waves from the expected azimuths has a mean-square deviation of 37.2°. The mean-square deviation is larger at 5 Hz (72.2°) and 20 Hz (48.8°). At 20 Hz, the main reason is increased scattering of the wave. Known causes for the large deviations observed at 5 Hz that were identified for some of the blasts are: confusion with surface waves from previous blasts, low signal-to-noise ratio (confusion with seismic noise), and locally produced disturbances.
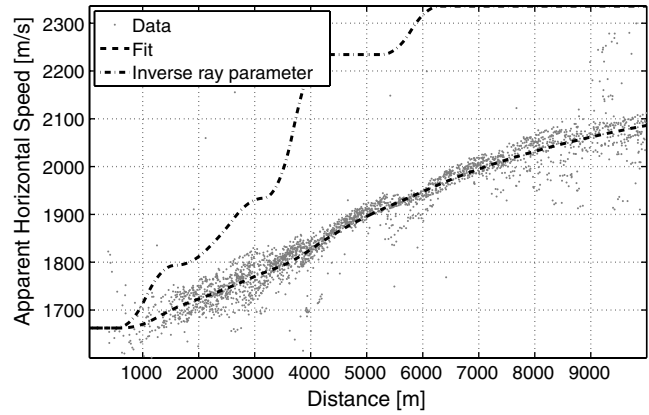
The observation of travel times (by a surface array) cannot yield a uniquely defined velocity profile $v(z)$. A problem occurs when the stratification includes hidden layers or low-velocity zones. Here, we will assume a monotonically increasing profile $v(z)$ with increasing depth z, which is built into our model by constraining the fit to the travel-time data such that it leads to a function $T(X)$ with negative second derivative. The travel-time data and the fit are shown in Figure 9. More details can be seen in Figure 10, where the ratios X/T of horizontal distances and travel times are shown. The figure also contains a plot of the inverse ray parameter.

Finally, the result for the velocity profile is displayed in Figure 11. Despite its high statistical significance due to the great number of blasts, the result should be taken with caution. The estimated profile could be subject to substantial systematic errors, depending on the validity of several assumptions. As mentioned, we assume that because the blasts originated from all directions, lateral homogeneities average out. Figure 1 shows that most shot holes were located north of the seismometers. This, combined with the structural dip mentioned in the section Local Geology, means that the deepest layers probed by waves from the most distant blasts may be up to 100 m deeper directly below the LIGO detector than indicated by our analysis. This needs to be taken into account if a more accurate estimation of local geology is required (although we believe that this error is not significant in the context of Newtonian-noise modelling). The assumption that exotic features like hidden layers and low-velocity zones do not exist at greater depths seems reasonable but is in fact impossible to test with our analysis methods. The borehole tests performed by Woodward-Clyde
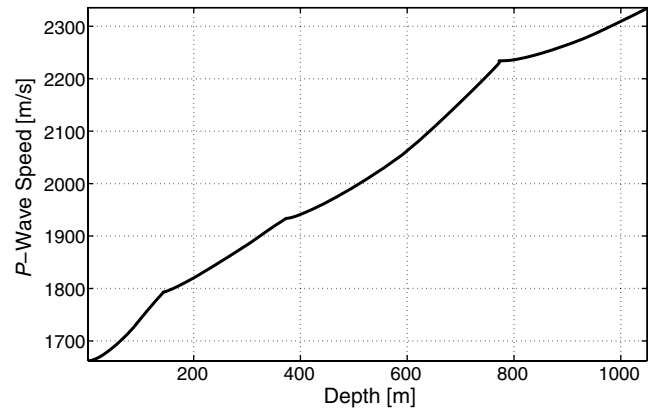

Figure 10. The travel-time data are plotted as X_i/T_i. The same quantity is shown for a constrained fit $T(X)$ to the data as discussed in the text. The inverse ray parameter dX/dT determines the seismic speeds of the horizontal stratification. One of the constraints ensures that the inverse ray parameter is a monotonically increasing function of horizontal distance.

Consultants (1995) identified low-velocity layers within the first 15 m of the ground, but there are no results for deeper layers relevant to the analysis in this section. The plot in Figure 10 shows discontinuities in the shape of collected data points that may indicate geological features unaccounted for by our simplified model or may simply be a consequence of local geology at the three stations. Alternative analyses (e.g., measurements of blast-pulse rise times) need to be carried out to further investigate this problem.

Seismic Attenuation

The attenuation of seismic waves can be parameterized by the Q value of the medium. Analyses of surface waves

Figure 9. The difference $\tau_i = T_i - p_0 X_i$ with constant apparent horizontal slowness $p_0 = 1/2100$ s/m, together with a constrained spline fit $\tau_k(X_k)$. The ray parameter is determined by the slope of the curve $d\tau/dX = p - p_0$. Because the slope decreases with increasing distance X, the ray parameter is monotonically decreasing (i.e., more distant blasts probe deeper and faster layers). Without the additional constraint to include the origin, the fit would intersect the time axis at negative values (independent of p_0), which has no physical explanation but is a consequence of measurement errors and scarcity of data from near shot holes.

Figure 11. The fit to the travel-time data was constrained to yield a monotonically increasing velocity–depth profile $v(z)$. At about 150, 370, and 770 m depth, the profile indicates discontinuities of the velocity gradient followed by a zone that is characterized by a slow increase of seismic speed. The deepest layer of the model has a depth of about 1 km. The discontinuities at 370 and 770 m are consistent with the extrapolated locations of the middle Miocene–upper Miocene–Pliocene transitions that were specified in Bebout and Gutiérrez (1983) for depths greater than 900 m.

and body P waves were carried out separately to obtain a Q value for the near-surface layers and one for the deeper layers.

As outlined in Carmichael (1989), the seismic signal k measured by seismometer i can be cast into the following form:

$$u_{ik}(f) = R_i(f)P_{ik}(f)S_k(f) \exp\left(-f \int_{ik} \mathrm{d}l\alpha_0\right). \quad (4)$$

This expression contains the response function of the sensor $R_i(f)$ that is common to all measured signals, and usually known to the experimenter, and the propagator $P_{ik}(f)$ that links the source function $S_k(f)$ to the seismic field at the seismometer. In the simplest case, the propagator describes a frequency-independent change in amplitude due to geometric damping and a change of the wave's complex phase. The path-integral term describes the damping of the wave, where the path integral is taken along the seismic ray and the damping factor α_0 can vary along the ray from the origin (k) to the sensor (i). Introducing the horizontal distance X travelled by the blast wave, one can rewrite the damping term in the form

$$\int_{ik} \mathrm{d}l\alpha_0 = X_{ik}\alpha_0(X_{ik}), \quad (5)$$

where $\alpha_0(X)$ is the damping averaged over the entire ray that extends over a horizontal distance X, again assuming lateral homogeneity.

Seismic damping will be estimated based on the spectral method presented in Quan and Harris (1997). The spectral method is basically a comparison of blast spectra measured at different distances. The overall amplitude decreases due to geometric spreading, but there is also a frequency-dependent change in spectral shape in accord with equation (4) and produced by exponential damping. The spectral method was originally derived for specific spectral shapes (e.g., Gaussian or rectangular). We will present it in a generalized form to show that it can be easily applied to arbitrary spectra.

Figure 12 shows the root power–spectral densities $r(f, X)$ of the blast waves as a function of horizontal propagation distance X. The plot exhibits a low-frequency regime at 0.4–10 Hz (determined by surface waves) and a high-frequency regime at 10–50 Hz (determined by body P waves). Because attenuation depends on wave type and because each wave type probes a different part of the ground, the attenuation will be analyzed for each regime separately. At first, we define the centroid $f_c(X)$ of a spectrum as

$$f_c(X) = \frac{\int_c \mathrm{d}f f r(f, X)}{\int_c \mathrm{d}f r(f, X)}, \quad (6)$$

where the integration is carried out over frequencies that are associated with either surface or body waves. The centroid is independent of geometric damping. We interpret a change in the centroid with distance as exponential damping. This is
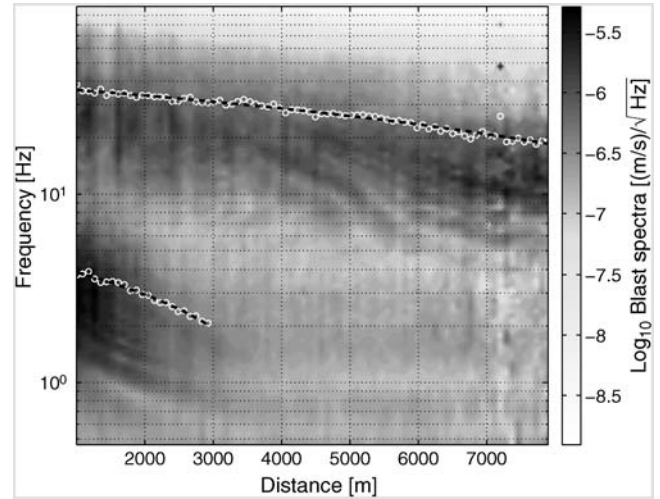
Figure 12. The root power–spectral density of blast waves as a function of horizontal distance between shot hole and seismometer. The spectrum can be divided into a high-frequency regime that is determined by the amplitudes of body compressional waves and a low-frequency regime that is determined by Rayleigh waves. The spectral shape in each regime is characterized by a centroid $f_c(X)$ and width $\sigma_c^2(X)$. The centroids calculated from the measured spectral densities are drawn as white circles, together with a polynomial fit (dashed curves, order $n = 2$).

clearly the case for the blast data, as can be seen in Figure 12, where the locations of the centroids are indicated with white circles together with quadratic fits. It follows that centroids of spectra measured at distances X_1 and X_2 are related according to

$$\begin{aligned}
\Delta f_c &= \frac{\int_c \mathrm{d}f f r(f, X_1) \exp(-f\Delta X\alpha_0)}{\int_c \mathrm{d}f r(f, X_1) \exp(-f\Delta X\alpha_0)} - f_c(X_1) \\
&\approx -\left[\frac{\int_c \mathrm{d}f f^2 r(f, X_1)}{\int_c \mathrm{d}f r(f, X_1)} - \left(\frac{\int_c \mathrm{d}f f r(f, X_1)}{\int_c \mathrm{d}f r(f, X_1)}\right)^2\right]\Delta X\alpha_0 \\
&= -\frac{\int_c \mathrm{d}f [f - f_c(X_1)]^2 r(f, X_1)}{\int_c \mathrm{d}f r(f, X_1)}\Delta X\alpha_0\kappa, \quad (7)
\end{aligned}$$

where $\Delta X \equiv X_2 - X_1$ and $\Delta f_c \equiv f_c(X_2) - f_c(X_1)$. The integrals and their fraction in the first line are expanded up to first order in ΔX. Equation (6) was applied to give the expected cancellation of zero-order terms. Equation (7) is based on the assumption that $f\Delta X\alpha_0 \ll 1$, but it would be straightforward to calculate higher-order corrections leading to a polynomial equation for α_0. In principle, one could also estimate α_0 numerically from the first line of equation (7) without further approximations. It is easy to show that higher-order corrections of the damping term are tightly linked to higher-order moments of the spectrum $r(f, X)$. For example, for the centroid as a function of distance, one can write

$$f_c(X_2) = -\partial_\epsilon \log\left[\int \mathrm{d}f r(f, X_1) \exp(-\epsilon f)\right]\bigg|_{\epsilon=\Delta X\alpha_0}, \quad (8)$$

where the logarithm is known from statistics as the cumulant moment-generating function $g(-\epsilon)$. In other words, if damping is approximated as a series in $(\Delta X \alpha_0)$, then the coefficient of the contribution $(\Delta X \alpha_0)^n$ is the $(n + 1)$-th cumulant of the spectrum $r(f, X)$; for example, the first cumulant is the mean, and the second cumulant is the variance. Therefore, the series can be stopped at $(\Delta X \alpha_0)$ when the spectrum has Gaussian shape. Equations similar to equation (8) can be derived to obtain the width or higher-order moments of the spectrum as a function of distance. It immediately follows that the width of a Gaussian-shaped blast spectrum does not change due to exponential damping.

Because the fraction of integrals in the second line of equation (7) has the form of a normalized second-order moment of the spectrum $r(f, X)$, we rewrite the equation into the form

$$\alpha_0(\Delta X) = -\frac{\Delta f_c / \Delta X}{\sigma_c^2}. \tag{9}$$

The function $\alpha_0(\Delta X)$ describes the damping of seismic waves that travelled a horizontal distance ΔX, and σ_c is the width of the spectrum at distance X_1, which will be 1 km in the following. Alternatively, the damping can be parameterized by the Q value of the medium:

$$Q(\Delta X) = \frac{\pi}{\alpha_0(\Delta X) c(X_2)}, = -\frac{\pi \sigma_c^2}{\Delta f_c / \Delta X c(X_2)}. \tag{10}$$

Here, we introduced the distance-dependent seismic speed $c(X_2)$ to account for the fact that body waves from distant shot holes probe deeper and faster layers than waves from closer shot holes. For body P waves, $c(X_2)$ is given by the fit to the average apparent horizontal speed shown in Figure 10. Our best knowledge of surface-wave speed comes from Figure 8. We will use a constant $c(X_2) = 205$ m/s to calculate the surface-wave attenuation. The estimated Q values are shown in Figure 13 and Table 1. Because the closest blasts included in this analysis have a distance of 1 km to a seismometer, one can derive from Figures 10 and 11 that the medium probed by the body waves lies below 100 m except for the last short section of the ray path just before the wave reaches the surface.

Previously published results for seismic damping are consistent with our values. In sedimentary sequences and for frequencies above 50 Hz, Q values were found to lie between about $Q = 30$ and $Q = 110$, although much higher Q were observed at greater depths (Carmicheal, 1989). Systematic errors caused by overly simplified geologies usually lead to an underestimation of the Q value. In Spencer et al. (1977, 1982), the influence of stratification was analyzed, and it was found that stratified media (what is called a cyclic system) can act as an additional low-pass filter that leads to a systematic underestimation of the Q value. A cyclic system requires fine layers with sudden impedance variations (i.e., variations in seismic speed) that gives rise to
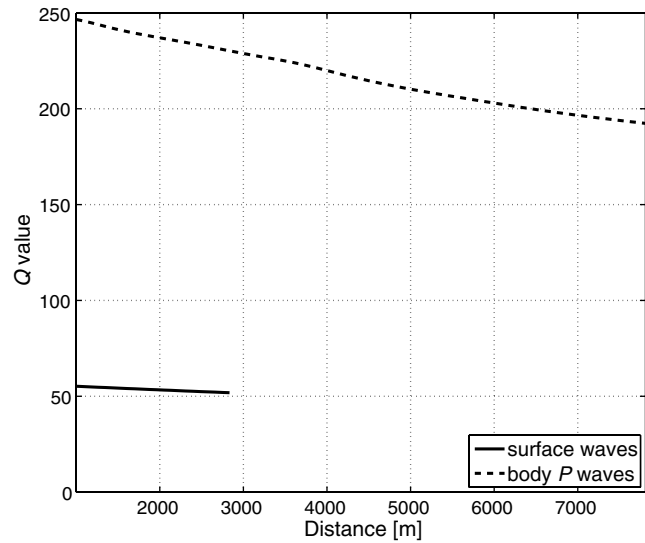
Figure 13. The Q values of near-surface layers are significantly smaller than the Q values of deeper layers probed by body waves. The decrease of Q values observed for body waves with increasing distance is likely caused by other frequency-dependent propagation effects related to the layered geology, as explained in the text.

multiple reflections and resonance effects. The decrease of Q values for P waves with increasing distance as shown in Figure 13 may be caused by this low-pass behavior because stratification has not been taken into account in our analysis. The presented method is also based on the assumption that the Q value is independent of frequency, at least within the ranges of 10–50 Hz for body waves and 0.4–10 Hz for the surface waves. The results reported in Thouvenot (1983) indicate that Q values can depend quite strongly on frequency, but one has to be careful interpreting the results because Q values were estimated by observing a decrease in seismic amplitude as a function of distance under the assumption that reflection or refraction from discontinuities do not occur. Because these effects are frequency dependent in layered geologies, as mentioned previously in this paper, the frequency dependence of Q may be overestimated. In our case, the problem could be resolved by estimating the Q value using an alternative technique (e.g., pulse broadening), but it should be noted that our method is still valid in the general case as a first-order approximation if the measured Q values are interpreted not only as spatial averages but also as averages over frequency (0.4–10 Hz and 10–50 Hz).

Table 1

Q Values at the Lower (1 km) and Upper (3 km or 8 km) Ends of the Distance Range in Figure 13

	Q (Closest Blasts)	Q (Farthest Blasts)
Surface waves	55	52
Body P waves	247	192

Conclusion

The analysis presented in this paper provides important parameters that will be required in future studies of Newtonian noise at the LIGO Livingston site. There are two aspects of the problem: constructing a sufficiently accurate Newtonian-noise model that maps seismic fields to gravity perturbations and designing the array that records the seismic data.

Because Newtonian noise results from an integration of the entire seismic field, and because a seismic array is finite in size and number, one has to infer seismic amplitudes at places where no seismic record is provided. For this problem, seismic attenuation needs to be known in order to correct amplitude estimates at more distant locations for exponential damping (although the influence of seismic attenuation on Newtonian-noise models has not been studied yet). Our highest seismic noise–to–instrumental noise (SNR) estimates of Q values are $Q = 250$ for the deeper ground and body waves and $Q = 50$ for Rayleigh waves propagating on unconsolidated sediments within the first meters to the surface.

The calculation of the velocity–depth profile for seismic compressional waves presented in the section Velocity-Depth Profile is based on many assumptions that, if incorrect, could potentially lead to significant systematic errors. In addition, the fit to the travel-time data had to be constrained, and certain features of the data (as shown in Figs. 9 and 10) are not properly accounted for by the fit. Certain methods used in seismic-refraction software take more details of the travel-time data into account and produce more reliable depth profiles. However, as pointed out before in this paper, a unique depth profile cannot be inferred from surface data alone irrespective of the applied method. One analysis that we propose for the future using the same data is to measure the pulse rise times of the blasts as part of a pulse-broadening tomography (Watanabe and Sassa, 1996). This would provide an independent method to estimate a velocity–depth profile that could be compared with our results.

The next step toward the construction of a Newtonian-noise model is to study the seismic-noise field by seismic arrays in the vicinity of the corner and end stations. The arrays are required to measure the mode content of the seismic-noise field (i.e., body waves versus surface waves) and shear waves versus compressional waves and to identify the modes that contribute most significantly to gravity perturbations at frequencies between 10 and 20 Hz. The array design depends mostly on our knowledge of seismic speeds of surface waves because surface waves are predicted to generate the main contribution to Newtonian noise at the surface. We found a Rayleigh-wave speed of 205 m/s and an indication for Rayleigh overtones with speeds between 300 and 400 m/s. Considering frequencies between 10 and 20 Hz, the diameter of the seismic array should not be smaller than 40 m, and the seismometer spacing should not exceed 5 m. These numbers are based on a simple geometrical argument, and one should keep in mind that maximum likelihood–based methods to estimate the spatial spectrum may have different requirements in terms of array size and density, depending on the SNR. In the end, the total number of seismometers also depends on the array configuration; that is, whether it has the shape of a circle, star, or spiral, which all have a different performance with respect to aliasing (Wathelet, 2005).

Data and Resources

Acknowledgments

References

Acernese, F., M. Alshourbagy, P. Amico, F. Antonucci, S. Aoudia, K. Arun, P. Astone, S. Avino, L. Baggio, G. Ballardin *et al.* (2008). Virgo status, *Classical Quant. Grav.* **25,** 184001.

Bebout, D. G., and D. R. Gutiérrez (1983). Regional cross sections, Louisiana Gulf Coast (eastern part), Folio Series No. 6 (maps), Baton Rouge, Louisiana Geological Survey.

Beccaria, M., M. Bernardini, S. Braccini, C. Bradaschia, A. Bozzi, C. Casciano, G. Cella, A. Ciampa, E. Cuocoy, G. Curci, E. D'Ambrosio *et al.* (1998). Relevance of Newtonian seismic noise for the VIRGO interferometer sensitivity, *Classical Quant. Grav* **15,** 3339–3362.

Carmichael, R. S. (1989). *Practical Handbook of Physical Properties of Rocks and Minerals*, CRC Press, Boca Raton, Florida, 741 pp.

Cutler, C., and K. S. Thorne (2002). An overview of gravitational-wave sources, available at http://arxiv.org/abs/gr-qc/0204090.

Harms, J., R. DeSalvo, S. Dorsher, and V. Mandic (2009a). Gravity-gradient subtraction in 3rd generation underground gravitational-wave detectors in homogeneous media, available at http://arxiv.org/abs/0910 .2774.

Harms, J., R. DeSalvo, S. Dorsher, and V. Mandic (2009b). Simulation of underground gravity gradients from stochastic seismic fields, *Phys. Rev. D* **80,** paper 122001.

Hild, S., S. Chelkowski, A. Freise, J. Franc, N. Morgado, R. Flaminio, and R. DeSalvo (2009). A xylophone configuration for a third-generation gravitational wave detector, *Classical Quant. Grav.* **27,** paper 015003.

Hughes, S. A., and K. S. Thorne (1998). Seismic gravity-gradient noise in interferometric gravitational-wave detectors, *Phys. Rev. D* **58,** paper 122002.

Laser Interferometer Gravitational-Wave Observatory (LIGO) Scientific Collaboration (2009). LIGO: the Laser Interferometer Gravitational-Wave Observatory, *Rep. Prog. Phys.* **72,** paper 076901.

Lück, H., M. Hewitson, P. Ajith, B. Allen, P. Aufmuth, C. Aulbert, Babak S., R. Balasubramanian, B. W. Barr, S. Berukoff *et al.* (2006). Status of the GEO600 detector, *Classical Quant. Grav.* **23,** S71–S78.

Quan, Y., and J. M. Harris (1997). Seismic attenuation tomography using the frequency shift method, *Geophysics* **62,** 895–905.

Saulson, P. R. (1984). Terrestrial gravitational noise on a gravitational wave antenna, *Phys. Rev. D* **30,** 732–736.

Smith, J. R. (for the Laser Interferometer Gravitational-Wave Observatory [LIGO] Scientific Collaboration) (2009). The path to the enhanced and advanced LIGO gravitational-wave detectors, *Classical Quant. Grav.* **26,** paper 114013.

Spencer, T. W., C. M. Edwards, and J. R. Sonnad (1977). Seismic wave attenuation in nonresolvable cyclic stratification, *Geophysics* **42,** 939–949.

Spencer, T. W., J. R. Sonnad, and T. M. Butler (1982). Seismic Q—stratigraphy or dissipation, *Geophysics* **47,** 16–24.

Tatsumi, D. (2008). TAMA300 interferometer development, *J. Phys. Conf.* **120,** paper 032011.

Thouvenot, F. (1983). Frequency dependence of the quality factor in the upper crust: A deep seismic sounding approach, *Geophys. J. Roy. Astr. Soc.* **73,** 427–447.

Watanabe, T., and K. Sassa (1996). Seismic attenuation tomography and its application to rock mass evaluation, *Int. J. Rock Mech. Min. Sci. Geomech. Abstr.* **33,** 467–477.

Wathelet, M. (2005). Array recordings of ambient vibrations: surface-wave inversion, *Ph.D. Thesis*, Université de Liège, Belgium.

Woodward-Clyde Consultants (1995). *Geotechnical Investigation of the LIGO site*, Livingston, Louisiana, 322 pp.

California Institute of Technology
1200 E. California Blvd
Pasadena, California 91125
    (J.H.)

Laser Interferometer Gravitational-Wave Observatory (LIGO)
Livingston Observatory
Livingston, Louisiana 70754
    (B.O.)